

# Sulfone-containing covalent organic frameworks for photocatalytic hydrogen evolution from water

Xiaoyan Wang<sup>1</sup>, Linjiang Chen<sup>1,2</sup>, Samantha Y. Chong<sup>1</sup>, Marc A. Little<sup>1</sup>, Yongzhen Wu<sup>3</sup>, Wei-Hong Zhu<sup>3</sup>, Rob Clowes<sup>1</sup>, Yong Yan<sup>1</sup>, Martijn A. Zwijnenburg<sup>4</sup>, Reiner Sebastian Sprick<sup>1</sup> and Andrew I. Cooper<sup>1,2\*</sup>

**Nature uses organic molecules for light harvesting and photosynthesis, but most man-made water splitting catalysts are inorganic semiconductors. Organic photocatalysts, while attractive because of their synthetic tunability, tend to have low quantum efficiencies for water splitting. Here we present a crystalline covalent organic framework (COF) based on a benzo-bis(benzothiophene sulfone) moiety that shows a much higher activity for photochemical hydrogen evolution than its amorphous or semicrystalline counterparts. The COF is stable under long-term visible irradiation and shows steady photochemical hydrogen evolution with a sacrificial electron donor for at least 50 hours. We attribute the high quantum efficiency of fused-sulfone-COF to its crystallinity, its strong visible light absorption, and its wettable, hydrophilic 3.2 nm mesopores. These pores allow the framework to be dye-sensitized, leading to a further 61% enhancement in the hydrogen evolution rate up to 16.3 mmol g<sup>-1</sup> h<sup>-1</sup>. The COF also retained its photocatalytic activity when cast as a thin film onto a support.**

Photocatalytic solar hydrogen production—or water splitting—offers an abundant clean energy source for the future. The use of dispersed, powdered photocatalysts or thin catalyst films is attractively simple, but, so far, no catalyst satisfies the combined requirements of cost, stability and solar-to-hydrogen efficiency. Since the first report of TiO<sub>2</sub> as a photocatalyst<sup>1</sup>, many inorganic semiconductors have been explored for water splitting, both in photoelectrochemical cells and as photocatalyst suspensions<sup>2–4</sup>. Recently, organic semiconductors have emerged as promising materials for photocatalytic hydrogen and oxygen evolution<sup>5–7</sup>. Poly(*p*-phenylene) was first reported as a photocatalyst for hydrogen evolution in 1985<sup>8,9</sup>, but its activity was poor and limited to the ultraviolet spectrum. Since then, more active organic materials have been reported as visible-light photocatalysts for hydrogen production using sacrificial donors. This started with carbon nitrides<sup>5,10</sup>, followed by poly(azomethine)s<sup>11</sup>, conjugated microporous polymers (CMPs)<sup>6,12,13</sup>, linear conjugated polymers<sup>12,14–16</sup> and covalent triazine-based frameworks (CTFs)<sup>17–19</sup>. Carbon nitrides were further developed into hybrid systems that facilitate overall water splitting to produce both hydrogen and oxygen, for example by including metal co-catalysts<sup>20</sup>. CMPs were also claimed to exhibit overall photocatalytic water splitting<sup>21</sup>. However, while it is possible to tune semiconductor properties such as the bandgap by modular copolymerization strategies<sup>6</sup>, organic materials such as carbon nitrides, conjugated polymers and CTFs lack long-range order (they are amorphous or semicrystalline<sup>17,22</sup>). This lack of order might limit the transport of photoactive charges to the catalyst surface<sup>23</sup>. More generally, it is challenging to construct atomistic structure–property relationships for materials where the 3D architecture is poorly defined.

Covalent organic frameworks (COFs)<sup>24–26</sup> are a class of organic materials that combine crystallinity, modular synthetic versatility,

highly accessible surface areas and, sometimes, good physicochemical stability<sup>27–30</sup>. With suitable building blocks and layered stacking sequences, COFs have been shown to have high charge-carrier mobilities<sup>31</sup>. So far, only a small number of COFs have been studied for their photocatalytic hydrogen evolution activity<sup>32,33</sup>. A hydrazone-based COF was reported by Lotsch and co-workers in 2014 to be active for sacrificial hydrogen production<sup>34</sup>, and this team subsequently reported a series of 2D azine COFs with impressive photocatalytic hydrogen evolution rates (HERs) of up to 1.7 mmol g<sup>-1</sup> h<sup>-1</sup> (N<sub>3</sub>-COF; Fig. 1a) using triethanolamine (TEOA) as a sacrificial donor and a Pt co-catalyst<sup>35,36</sup>. Recently, Thomas and co-workers described a diacetylene-functionalized COF with good hydrogen evolution activity<sup>37</sup>. Kurongot and Banerjee reported a cadmium sulfide–COF composite material with a higher HER of 3.68 mmol g<sup>-1</sup> h<sup>-1</sup> using lactic acid as the sacrificial agent<sup>32</sup>, although the COF was the minor component in that composite (90 wt% CdS). Porous COFs can also be modified after synthesis: for example, a molecular cobaloxime co-catalyst was introduced into an azine COF to give a HER of 0.78 mmol g<sup>-1</sup> h<sup>-1</sup> (ref. 38). HERs for a given catalyst can vary substantially in different laboratories depending on the optical set-up; with that caveat in mind, N<sub>3</sub>-COF is the most active, unmodified COF for sacrificial hydrogen evolution reported so far<sup>35</sup>. COF films have also been used as carbon dioxide reduction catalysts<sup>39</sup> and, in film form, as photoelectrodes for light-driven water splitting<sup>40</sup>.

We have shown previously that a linear conjugated copolymer, P7 (Fig. 1b), exhibits HERs of up to 1.49 mmol g<sup>-1</sup> h<sup>-1</sup> with a sacrificial amine donor under visible irradiation ( $\lambda > 420$  nm)<sup>16</sup>; that is, close to the value reported for N<sub>3</sub>-COF<sup>35</sup>. We ascribed this to the rigid, planar dibenzo[*b,d*]thiophene sulfone (DBTS) unit in the P7 copolymer. Homopolymerization of this DBTS monomer gives a polymer, P10 (Fig. 1b), with an even higher HER (3.26 mmol g<sup>-1</sup> h<sup>-1</sup>,

<sup>1</sup>Department of Chemistry and Materials Innovation Factory, University of Liverpool, Liverpool, UK. <sup>2</sup>Leverhulme Research Centre for Functional Materials Design, Materials Innovation Factory and Department of Chemistry, University of Liverpool, Liverpool, UK. <sup>3</sup>Key Laboratory for Advanced Materials and Institute of Fine Chemicals, East China University of Science and Technology, Shanghai, China. <sup>4</sup>Department of Chemistry, University College London, London, UK. \*e-mail: [aicooper@liverpool.ac.uk](mailto:aicooper@liverpool.ac.uk)

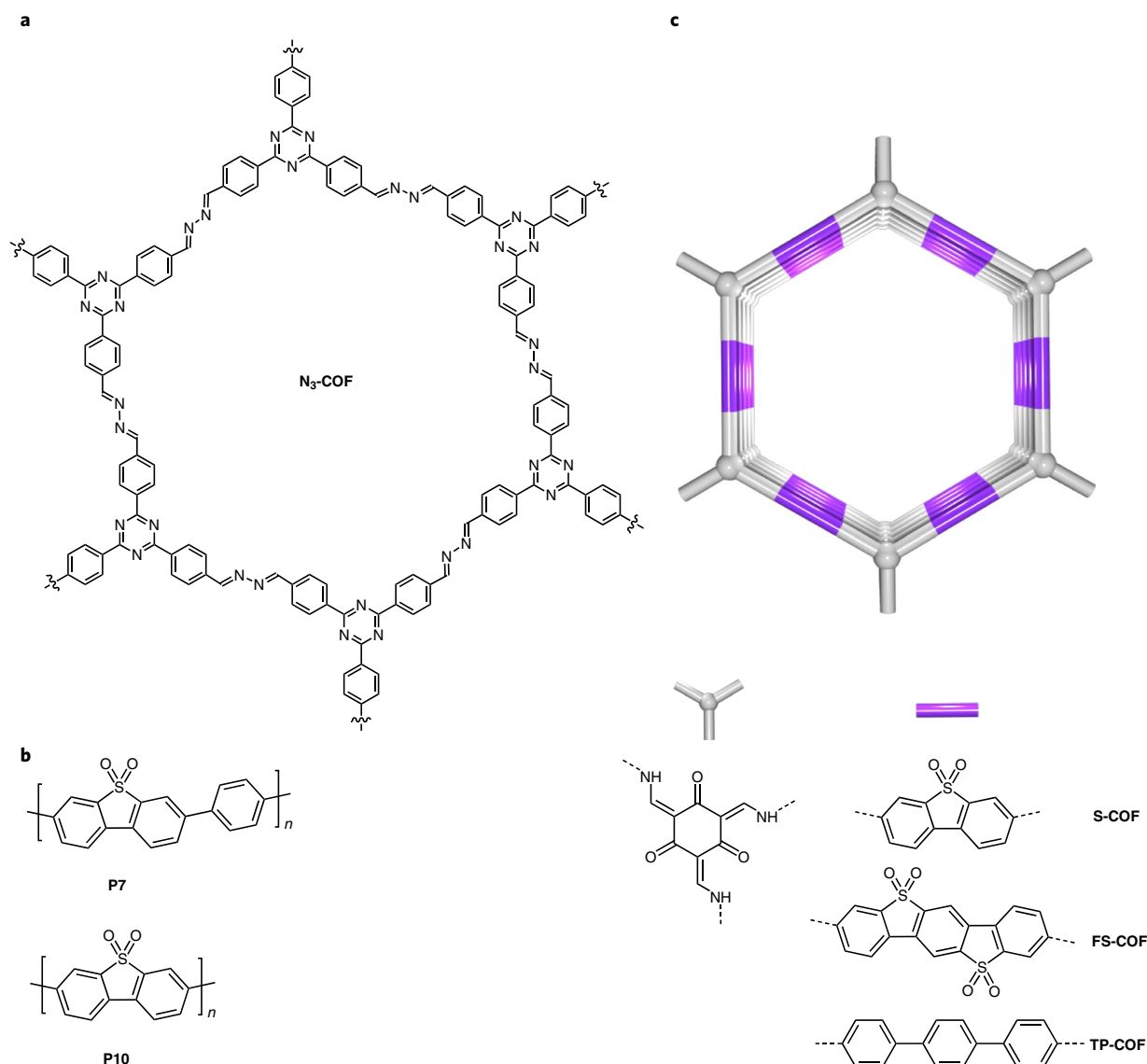


**Fig. 1 | Chemical structures of the organic photocatalysts studied here. a, b,** Chemical structures of previously reported photocatalysts  $N_3$ -COF<sup>35</sup> (a), P7<sup>16</sup> and P10 (b). **c,** Chemical structures of the COF photocatalysts reported in this work: S-COF, FS-COF and TP-COF.

Supplementary Fig. 95). Unlike COFs, these polymers are semicrystalline: they are also non-porous and insoluble, which precludes post-synthetic modification strategies. Here, we set out to incorporate the DBTS unit into ordered COFs to investigate the influence of crystallinity and porosity on the photocatalytic activity. This led to a new crystalline organic material, **FS-COF** (where FS is fused sulfone), which is a better photocatalyst than equivalent amorphous or semicrystalline conjugated polymers. **FS-COF** also exhibits higher HERs than other COFs studied so far—up to  $16.3 \text{ mmol g}^{-1} \text{ h}^{-1}$  when dye-sensitized, which is almost ten times higher than  $N_3$ -COF.

## Results and discussion

**COF synthesis and characterization.** Three COFs—S-COF, FS-COF and TP-COF (Fig. 1c)—were synthesized via a Schiff-base condensation reaction of 1,3,5-triformylphloroglucinol with aromatic diamines (Supplementary Figs. 1–3). The products undergo an irreversible keto-enol tautomerization, which enhances their chemical stability<sup>29</sup>. We used 3,7-diaminodibenzo[*b,d*]thiophene sulfone (SA) as the monomer for S-COF, which is a crystalline COF analogue of semicrystalline polymers P7 and P10 (Fig. 1b). We also

used 3,9-diamino-benzo[1,2-*b*:4,5-*b'*]bis[1]benzothiophene sulfone (FSA) to produce FS-COF, which has fused, extended planar linkers. TP-COF was synthesized as before<sup>41</sup>; it was prepared from 4,4''-diamino-*p*-terphenyl (TPA) and it is, in essence, FS-COF minus the sulfone moieties (Fig. 1c).

All three linkers gave rise to crystalline COFs (Fig. 2 and Supplementary Figs. 24–28). Based on powder X-ray diffraction (PXRD) data, FS-COF (Fig. 2c) appeared to have more long-range order than either S-COF (Fig. 2d) or TP-COF (Supplementary Fig. 28). This might be because the C–N bonds in the FSA monomer are parallel, whereas the angle between the C–N bonds in the SA monomer is  $\sim 163^\circ$  (Supplementary Fig. 14), and hence the regular hexagonal framework in FS-COF may be less sensitive than S-COF to the insertion of linkers in the ‘wrong’ geometry. More effective  $\pi$ – $\pi$  stacking between the fused, planar FSA linkers might also help to stabilize FS-COF.

PXRD was used to characterize the three COFs. FS-COF exhibited diffraction peaks at 2.71, 4.73, 5.52 and 7.35°, which were assigned to the (100), (110), (200) and (210) planes, respectively (Fig. 2c). The broad intensity at 25.19° was assigned to the (001)

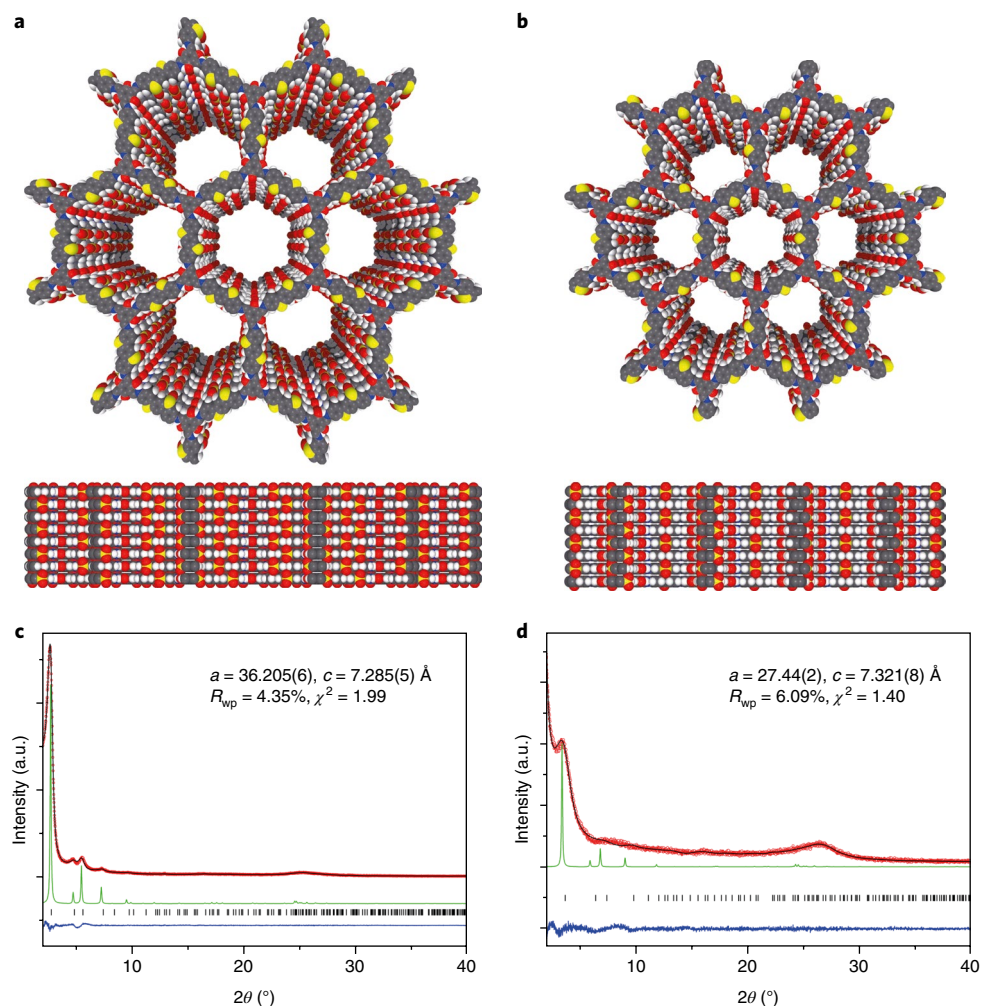


**Fig. 2 | Crystal structures of FS-COF and S-COF.** **a,b**, Structural models for FS-COF (**a**) and S-COF (**b**) with perfectly eclipsed AA stacking patterns, shown parallel to the pore channel along the crystallographic  $c$  axis (top) and parallel to the hexagonal layers (bottom). The pores of both COFs are lined with oxygen atoms. Grey, white, blue, red and yellow atoms represent carbon, hydrogen, nitrogen, oxygen and sulfur, respectively. **c,d**, Experimental diffraction patterns (red), profiles calculated from Le Bail fitting (black) and residual (blue), and pattern simulated from the structural model (green) for FS-COF (**c**) and S-COF (**d**). Reflection positions are shown by tick marks.

plane, corresponding to a layer spacing of 3.53 Å. Multiple reflections indicate that FS-COF has high periodicity in three dimensions. Le Bail refinements confirmed that the diffraction pattern was consistent with a primitive hexagonal lattice with unit cell parameters ( $a = b = 36.205(6)$  Å,  $c = 7.285(5)$  Å) similar to an idealized eclipsed model of FS-COF (Fig. 2a, top). S-COF exhibited lower crystallinity, indicated by the broadened diffraction profile. The observable diffraction intensities can be accounted for by a primitive hexagonal structure with an in-plane lattice parameter of 27.44(2) Å and a  $\pi$ -stacking distance of  $\sim 3.7$  Å. Based on both laboratory and synchrotron XRD data (Supplementary Figs. 24–27), we propose that FS-COF and S-COF have AA layer stackings (Fig. 1c), rather than AB stacking. However, there are a variety of possible AA stacking patterns (Supplementary Fig. 93), and the X-ray data do not allow us to distinguish between these (Supplementary Figs. 25 and 26). For the purposes of structural comparisons with experimental data, we refer to the idealized, perfectly eclipsed AA stacking patterns (Fig. 2a,b) because properties such as porosity are not greatly affected by small shifts in the relative orientation of the layers. By contrast, calculations that are discussed later suggest that the electronic structure of FS-COF is quite strongly affected by small changes to the AA layer stacking.

The porosity of these COFs was assessed by nitrogen sorption measurements at 77.3 K. The Brunauer–Emmett–Teller (BET) surface areas of FS-COF, S-COF and TP-COF were found to be 1,288, 985 and 919 m<sup>2</sup> g<sup>−1</sup>, respectively. The measured surface area for FS-COF equates to 78% of the calculated nitrogen-accessible surface area for the idealized, eclipsed structure shown in Fig. 2a (1,652 m<sup>2</sup> g<sup>−1</sup>). The experimental surface areas for the two less crystalline COFs were lower than the idealized, calculated values (1,690 and 2,172 m<sup>2</sup> g<sup>−1</sup> for S-COF and TP-COF), although both materials were still microporous. The pore diameters derived for FS-COF, S-COF and TP-COF by fitting nonlocal density functional theory (DFT) models to the N<sub>2</sub> isotherms were 27.6, 22.8 and 29.0 Å, respectively. All COFs gave rise to nitrogen isotherms with shapes consistent with mesoporosity and sequential, multilayer pore filling (Fig. 3a and Supplementary Figs. 18–20).

High-resolution transmission electron microscopy (HR-TEM) images of FS-COF (Fig. 3b) confirmed that it has an ordered, hexagonal pore structure oriented along the crystallographic  $c$  axis with a periodicity of  $\sim 3.0$  nm (area outlined in red, Fig. 3b), which is consistent with the in-plane pore channels of 3.2 nm in the proposed AA-stacked COF structure. S-COF and TP-COF exhibited no such clear, ordered domains when analysed by HR-TEM (Supplementary

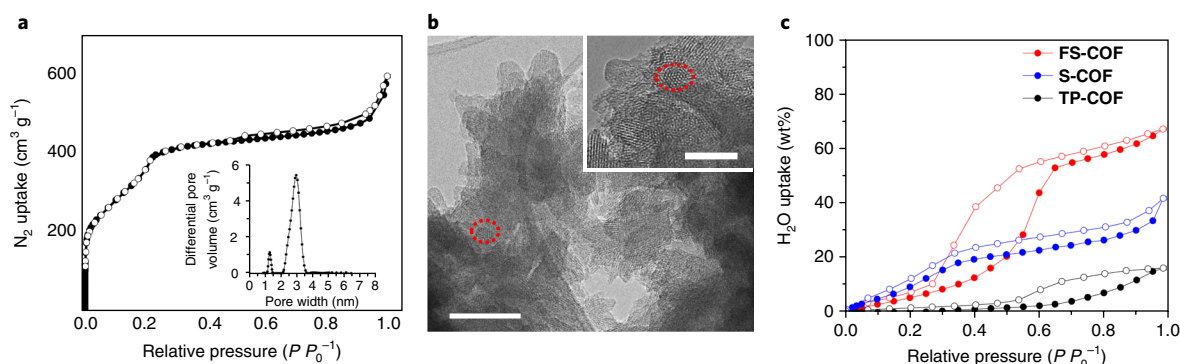


**Fig. 3 | Evidence for ordered, wettable mesopores in FS-COF.** **a**, Nitrogen adsorption isotherm (filled symbols) and desorption isotherm (open symbols) for FS-COF recorded at 77.3 K. Inset: profile of the calculated pore size distribution for FS-COF. **b**, HR-TEM image of FS-COF. The hexagonal pore structure with a periodicity of  $\sim 3.0$  nm is indicated by the dashed red outline. Scale bars, 50 nm (inset) and 100 nm (main). **c**, Water adsorption isotherms (filled symbols) and desorption isotherms (open symbols) for FS-COF, S-COF and TP-COF, measured at 293 K.  $P/P_0^{-1}$ , vapor pressure over saturation pressure.

Fig. 31). Atomic force microscopy (AFM) images of FS-COF deposited onto silicon wafers from water suspensions also show that this COF can be partially exfoliated into thin stacks, albeit not single layers, with thicknesses ranging from 5 to 25 nm (Supplementary Fig. 33).

UV-vis reflectance spectra of the COFs were measured in the solid state, and the absorption onset was found to be 670, 590 and 540 nm for FS-COF, S-COF and TP-COF, respectively (Fig. 4a). The onsets for FS-COF, S-COF and TP-COF are redshifted by 70, 45 and 90 nm, respectively, compared to their diamine monomers. The UV-vis spectra of an amorphous analogue FS-P, discussed below, show a blueshift compared with FS-COF, but it also exhibits a redshifted absorption compared to the diamine monomer. FS-COF absorbs more light in the visible spectrum and shows a significant redshift in its absorption onset compared to the corresponding linear dibenzo[*b,d*]thiophene sulfone-based polymers, P7 and P10, by 210 and 184 nm.

**Photocatalysis experiments.** We next investigated the activity of these COFs for photocatalytic water reduction using ascorbic acid as a sacrificial electron donor (SED) and Pt as a co-catalyst. All materials evolved hydrogen under visible light ( $\lambda > 420$  nm, Fig. 4b) and the average HERs were determined to be  $1.6 \text{ mmol g}^{-1} \text{ h}^{-1}$  for TP-COF,  $4.44 \text{ mmol g}^{-1} \text{ h}^{-1}$  for S-COF and  $10.1 \text{ mmol g}^{-1} \text{ h}^{-1}$  for FS-COF. As in previous reports for porous titania glasses<sup>42</sup>, strontium titanate<sup>43</sup> and carbon nitride<sup>5</sup>, we observed the production of smaller, although still significant, quantities of hydrogen without the addition of Pt for S-COF and FS-COF with rates of 0.6 and  $1.32 \text{ mmol g}^{-1} \text{ h}^{-1}$ , respectively. No hydrogen production was observed for TP-COF without Pt. The mass-normalized HER for FS-COF of  $10.1 \text{ mmol g}^{-1} \text{ h}^{-1}$  is the highest reported for a photocatalytically active COF (Table 1). This rate is 22 times higher than for N<sub>3</sub>-COF ( $0.47 \text{ mmol g}^{-1} \text{ h}^{-1}$ ), as measured by us under identical conditions over 5 h (with ascorbic acid), and around six times higher than the optimized rate reported for N<sub>3</sub>-COF by Vyas and colleagues using triethanolamine as a sacrificial donor<sup>35</sup>.

An external quantum efficiency (EQE) of 3.2% was determined for FS-COF at 420 nm (violet light), whereas 1.3% was reported for the diacetylene COF<sup>37</sup> at 420 nm and 0.44% for N<sub>3</sub>-COF at 450 nm, both using TEOA as a SED<sup>35</sup>. At even longer wavelengths (600 nm, orange light), FS-COF still displayed an EQE of 0.6% (Supplementary Fig. 40).

Longer-term photolysis experiments for FS-COF with up to 50 hours of visible light irradiation ( $\lambda > 420$  nm, Fig. 4c) showed no significant decrease in the catalytic performance over time, suggesting good stability. No changes to the PXRD patterns were

observed after long-term irradiation, showing that the crystallinity was retained (Supplementary Fig. 49). For comparison, we estimate that the 50-hour photolysis reported for N<sub>3</sub>-COF<sup>35</sup>, also using ascorbic acid as a sacrificial donor, yielded an average HER of  $\sim 0.08 \text{ mmol g}^{-1} \text{ h}^{-1}$  (Supplementary Fig. 63 in ref. 35), about 125 times lower than we observe for FS-COF.

The marked difference in catalytic activity between FS-COF and the isostructural framework TP-COF can be explained, at least in part, by the redshift in the absorption onset, which allows FS-COF to absorb more visible photons. The partial exfoliation of FS-COF may also contribute<sup>10,44</sup>. The higher BET surface area of  $1,288 \text{ m}^2 \text{ g}^{-1}$  for FS-COF versus  $919 \text{ m}^2 \text{ g}^{-1}$  for TP-COF might also enhance the availability of photogenerated charges for water reduction. For context, diffusion lengths of up to  $\sim 10$  nm have been reported for thin films of conjugated polymers<sup>45–47</sup>; hence, photogenerated charges produced inside non-porous particles much larger than 10 nm may not reach the particle surface.

Introducing sulfone groups results in much lower contact angles with pure water for FS-COF ( $23.6^\circ$ ) and S-COF ( $43.7^\circ$ ) in comparison with TP-COF ( $59.7^\circ$ ) and N<sub>3</sub>-COF ( $53.4^\circ$ ). These contact angles are low for organic materials: for reference, most organic polymers have contact angles in the range  $60$ – $110^\circ$ , and poly(vinyl alcohol) has a contact angle of  $\sim 51^\circ$  (ref. 48). Water vapour uptake measurements (Fig. 3c) show type II isotherms for FS-COF, S-COF and TP-COF. Functionalized FS-COF and S-COF adsorb 67 and 42 wt% water at 293 K and 22.9 mbar; by comparison, TP-COF adsorbs only 16 wt% water under the same conditions. This is due to water condensation<sup>49</sup> within the mesopores of FS-COF, which are decorated with a large number of polarized heteroatoms (Fig. 2a). Wetting matters in aqueous photocatalysis because particle dispersibility and favourable interactions with water and the sacrificial donor are required for good photocatalytic performance. The water isotherm for FS-COF shows that the internal pore structure of the material is accessible to water, as well as the external surface, thus increasing the number of potential sites for photocatalytic water reduction.

Besides light absorption, particle size and wettability, crystallinity might be important in the catalytic performance of FS-COF. In particular, the eclipsed AA layered structure of FS-COF (Fig. 2a) might facilitate charge carrier transport in the material, although it is not possible at this stage to deconvolute this from other factors, such as surface area. Increased long-range order in carbon nitride has been reported to improve photocatalytic activity by enhancing charge transport to active sites<sup>22</sup>. In this study, both S-COF and FS-COF strongly outperformed the corresponding semicrystalline



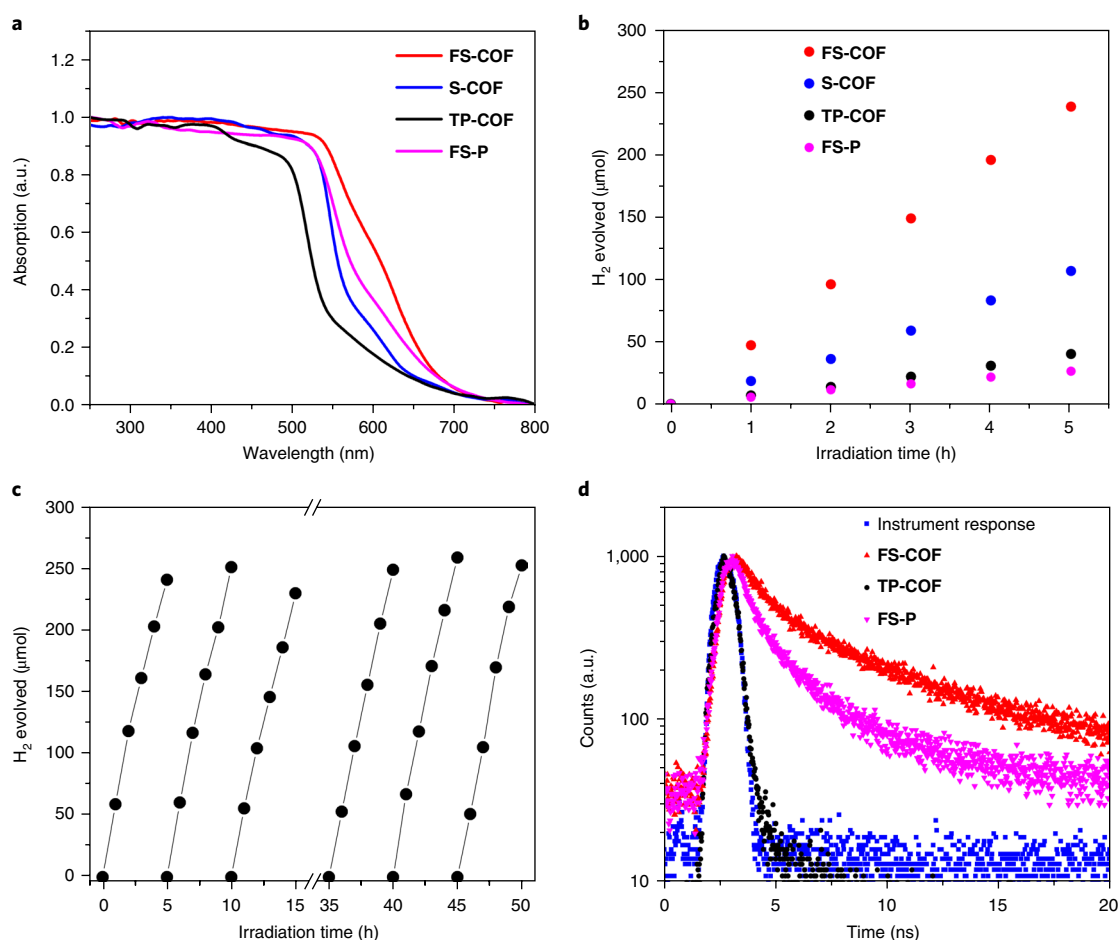


**Fig. 4 | Optical properties, HERs and excited-state lifetimes for the photocatalysts.** **a**, UV-vis absorption spectra for **FS-COF**, **S-COF**, **TP-COF** and **FS-P** measured in the solid state. **b**, Time course for photocatalytic  $\text{H}_2$  production using visible light for **FS-COF**, **S-COF**, **TP-COF** and **FS-P** (5 mg catalyst in water, 5  $\mu\text{l}$  (8 wt%  $\text{H}_2\text{PtCl}_6$ ), 0.1 M ascorbic acid,  $\lambda > 420$  nm). **c**,  $\text{H}_2$  production using visible light for **FS-COF** over 50 h total photolysis (5 mg catalyst in water, 5  $\mu\text{l}$  (8 wt%  $\text{H}_2\text{PtCl}_6$ ), 0.1 M ascorbic acid,  $\lambda > 420$  nm). The sample was degassed after 5 and 10 h to prevent saturation of the detector, then left under continuous illumination for 20 h and again degassed after 40 and 45 h. After 35 h, 1.25 mmol of ascorbic acid was added. **d**, Time-correlated single-photon counting experiments for **TP-COF**, **FS-COF** and **FS-P** in water. Samples were excited with a  $\lambda_{\text{exc}} = 370.5$  nm laser and emission was measured at  $\lambda_{\text{em}} = 550$  nm.

conjugated co-polymers **P7**<sup>16</sup> and **P10** that were the inspiration for these frameworks (Fig. 1 and Table 1). Under comparable conditions, **FS-COF** is around twelve times more active than **P7**, and seven times more active than **P10** (Table 1).

To further investigate the effect of crystallinity on photocatalytic performance, we synthesized **FS-P**, an almost amorphous analogue of **FS-COF** (Supplementary Fig. 29). We did this by carrying out the synthesis using 1,2-dichlorobenzene as the solvent, rather than a mixture of 1,4-dioxane and mesitylene (Supplementary Section 2). Amorphous **FS-P** showed much lower photocatalytic activity ( $\lambda > 420$  nm) and a HER of only  $1.12 \text{ mmol g}^{-1} \text{ h}^{-1}$ —nine times lower than **FS-COF**. **FS-P** showed a slightly blueshifted absorption onset (Fig. 4a) relative to **FS-COF**, possibly because the delocalization that arises from  $\pi$ - $\pi$  stacking in **FS-COF** is disrupted in this amorphous analogue, although its visible light absorption profile is still more favourable than those of **S-COF** or **TP-COF**. The low activity of **FS-P** may also be related to its reduced surface area ( $209 \text{ m}^2 \text{ g}^{-1}$ ) and a lower degree of condensation in the amorphous polymer. Weak absorption bands were observed in the Fourier transform infrared spectrum at  $3,371$  and  $3,473 \text{ cm}^{-1}$ , which are probably due to amine end groups<sup>29</sup>. Another important factor could be the particle size of the in situ deposited Pt co-catalyst: **FS-COF** has well-defined 3-nm-sized Pt nanoparticles on its surface (Supplementary Fig. 32), and

it is possible that the size is controlled by the uniform mesopores in the COF. By contrast, undefined micrometre-sized Pt aggregates were formed on the surface of amorphous **FS-P**.

We used time-correlated single-photon counting (TCSPC) to estimate the excited-state lifetimes for these materials in aqueous suspensions (Fig. 4d). The average weighted lifetime of **FS-COF** ( $\tau_{\text{avg}} = 5.56$  ns) was estimated to be significantly longer than that of **TP-COF** ( $\tau_{\text{avg}} = 0.25$  ns) or **FS-P** ( $\tau_{\text{avg}} = 2.21$  ns), which correlates with the higher photocatalytic performance observed for **FS-COF**.

**Computational studies.** For a COF to act as a hydrogen evolution photocatalyst, it must absorb light efficiently over a broad range in the visible spectrum as well transporting the electron-hole pairs, or excitons, that are formed following light absorption. The COF must also thermodynamically drive the reduction of protons and the oxidation of water—or in this study, the SED, ascorbic acid. To achieve this, the electron affinity (EA) of the COF or its exciton ionization potential ( $\text{IP}^*$ ) and the ionization potential (IP) of the COF or its exciton electron affinity ( $\text{EA}^*$ ) should straddle the proton reduction and water/SED oxidation potentials<sup>50</sup>. Because the potentials of a polymer are difficult to measure experimentally<sup>51</sup>, we instead predicted them computationally using DFT. We did this using two different approaches: cluster calculations on representative fragments

**Table 1 | Photophysical properties and HERs for the COF photocatalysts**

Photocatalyst	Degree of crystallinity	Optical gap <sup>b</sup> (eV)	HER <sup>c</sup> (mmol g <sup>-1</sup> h <sup>-1</sup> )	HER relative to FS-COF (%)
TP-COF <sup>a</sup>	Crystalline	2.28	1.60 ± (0.08)	16
S-COF <sup>a</sup>	Crystalline	2.10	4.44 ± (0.14)	43
FS-COF <sup>a</sup>	Crystalline	1.85	10.1 ± (0.3)	–
FS-P <sup>a</sup>	Amorphous	1.88	1.12 ± (0.16)	11
N <sub>3</sub> -COF <sup>35</sup>	Crystalline	2.60	0.47 ± (0.06)	4.6
P7 <sup>16</sup>	Semicrystalline	2.70	0.84 ± (0.06) <sup>d</sup>	8.3
P10	Semicrystalline	2.55	1.48 ± (0.1) <sup>d</sup>	15
FS-COF+W55F <sup>a</sup>	Crystalline	<sup>e</sup>	16.3 ± (0.29)	161
FS-COF+Eosin Y <sup>e</sup>	Crystalline	<sup>e</sup>	16.1 ± (0.34)	159
FS-P+W55F <sup>a</sup>	Amorphous	<sup>e</sup>	0.23 ± (0.03)	2.3
FS-P+Eosin Y <sup>e</sup>	Amorphous	<sup>e</sup>	0.58 ± (0.08)	5.8

<sup>a</sup>This work. <sup>b</sup>Calculated from the onset of the solid absorption spectrum. <sup>c</sup>All rates measured using the same instruments, optical set-up and reaction conditions: 5 mg COF catalyst, 5 µl (8 wt% H<sub>2</sub>PTCl<sub>6</sub>), 25 ml ascorbic acid aqueous solution (0.1 M), 300 W Xe light source equipped with λ > 420 nm cutoff filter. HERs based on average over 5 h irradiation and normalized to the COF mass. <sup>d</sup>As for <sup>c</sup>, but with no additional Pt catalyst added (Supplementary Fig. 35); HER for P10 in the presence of Pt was 1.92 mmol g<sup>-1</sup> h<sup>-1</sup>. <sup>e</sup>The effective optical gap was not measurable due to the intense absorption of the organic dye.

of the COFs embedded in a dielectric continuum to model the COF–water interface, and periodic calculations on COF crystal structures. These two approaches complement each other. By necessity, the periodic calculations approximate the IP and EA by the Kohn–Sham valence band maximum (VBM) and conduction band minimum (CBM). Hence, these calculations cannot describe the effect of immersing the COF in water, but they do take into account the influence of layer stacking. Cluster calculations are limited to a fragment, but unlike the periodic calculations, they describe the effect of water and allow us to calculate the exciton potentials and the exciton binding energy (EBE). The latter is important for polymers, where the EBE is generally large relative to  $kT$  (26 meV at room temperature), such that spontaneous dissociation of excitons into free electrons and holes is unlikely.

The cluster DFT (B3LYP) calculations on fragments embedded in a continuum with the relative dielectric permittivity of water predict that S-COF, FS-COF and TP-COF should all have substantial thermodynamic driving forces for proton reduction (Fig. 5a,b). Water oxidation is predicted to be endergonic or negligibly exergonic, providing a thermodynamic explanation for the inability of these materials to drive hydrogen evolution without a sacrificial agent. Ascorbic acid was used as a SED because its one-hole and two-hole oxidation potentials are more negative than the water oxidation potential, meaning it is more easily oxidized (Fig. 5a).

Cluster calculations for N<sub>3</sub>-COF (Fig. 5a,b) suggest a different picture. While the IP and EA of N<sub>3</sub>(L) straddle both water splitting half-reaction potentials, suggesting a driving force for overall water splitting, the EA\* and IP\* do not; this means that overall water splitting is still not thermodynamically favoured without bulk exciton dissociation—and the EBE is predicted to be as large as 0.92 eV. Calculations using range-separated density functionals also suggest that the EBE in N<sub>3</sub>-COF is large (Supplementary Fig. 91). The IP\* of N<sub>3</sub>(L) is only marginally more negative than the potential of proton reduction, and the EA\* is marginally more positive than the potential of the one-hole oxidation of ascorbic acid. The relatively low photocatalytic activity of N<sub>3</sub>-COF with ascorbic acid might therefore be linked to the combined effects of difficult exciton dissociation in

the bulk material and the small driving forces associated with exciton dissociation at the photocatalyst–solution interface.

Next, periodic DFT (HSE06) calculations were performed to investigate the electronic structures of the COF crystals. The position of the VBM and CBM for each COF crystal structure was referenced to a common vacuum level (Fig. 5c), determined by the value of the electrostatic potential at the centre of an internal pore. Both eclipsed (AA) and staggered (AB) stacking sequences were considered for S-COF, FS-COF and TP-COF (Fig. 5d); the eclipsed AA layered structure of N<sub>3</sub>-COF was also included for comparison. Our periodic results corroborate the molecular fragment picture; all of these COF materials are predicted, in certain AA packings, to be thermodynamically able to reduce protons and oxidize ascorbic acid, in line with experiments. The exact positions of the VBM and CBM for FS-COF were found to be sensitive to the small changes to the crystal structure, and this is most likely true for the other COFs as well. The CBM of the idealized, eclipsed AA-stacked FS-COF structure lies, in fact, below the proton reduction potential: hence, in the absence of water at least, this structure is not predicted to drive proton reduction. However, calculations show that minor levels of disorder, such as small offsets between neighbouring layers or partial/full flipping of the FS linkers in alternating layers, can alter the band-edge positions (black horizontal lines in Fig. 5c; Supplementary Fig. 93). All of these possible AA-stacked structure models are close in computed total lattice energy (Supplementary Table 7) and we cannot distinguish between them using either laboratory or synchrotron PXRD data (Supplementary Fig. 26). These calculations, coupled with the photocatalytic proton reduction observed for FS-COF, suggest that the crystal packing might not be exclusively the idealized AA stacking, although we note that the effect of water, as discussed above, cannot be included in these periodic calculations.

As observed experimentally, calculations predict correctly that FS-COF has the smallest optical gap among the four COF materials studied here and thus, probably, the largest rates of visible photon absorption and exciton generation. This is combined with favourably positioned IP/EA\*/VBM and EA/IP\*/CBM levels, at least for certain AA packings, to sustain a driving force for both redox half-reactions. Other factors may also contribute to the photocatalytic performance of FS-COF, such as, as discussed above, its strong affinity for water (Fig. 3c), good wettability (Supplementary Fig. 34), well-dispersed Pt co-catalyst particles (Supplementary Fig. 32), and the longer excited-state lifetime in this material (Fig. 4d).

**Dye sensitization.** The ordered mesoporosity in these frameworks offers various opportunities for post-synthetic modification. For example, we explored the dye sensitization of FS-COF with the goal of further enhancing its photocatalytic performance<sup>52</sup>. Addition of 2',7'-dichlorofluorescein (Supplementary Fig. 75) reduced the photocatalytic performance of FS-COF, while Rose Bengal (sodium salt of 4,5,6,7-tetrachloro-2',4',5',7'-tetraiodofluorescein) slightly improved the performance. However, when Eosin Y (2',4',5',7'-tetrabromofluorescein) was added, the HERs for FS-COF were enhanced by up to 60%; from 10.1 to 13 mmol g<sup>-1</sup> h<sup>-1</sup> (10 mg dye, 5 mg of FS-COF) and to 16.1 mmol g<sup>-1</sup> h<sup>-1</sup> when 20 mg of the dye was added. Further increases in the dye loading reduced the catalytic rate (Supplementary Fig. 76). By contrast, the HER of 5 mg of amorphous FS-P was reduced from 1.1 to 0.58 mmol g<sup>-1</sup> h<sup>-1</sup> in the presence of 20 mg of Eosin Y. The absorption spectrum of Eosin Y overlaps with the absorption spectrum of FS-COF, so the addition of dye probably enhances the total absorption cross-section of the system. Similarly, when a larger amount of FS-COF was used with no dye, then a similar increase in the HER was observed (12.9 mmol g<sup>-1</sup> h<sup>-1</sup> for 10 mg FS-COF versus 10.1 mmol g<sup>-1</sup> h<sup>-1</sup> for 5 mg FS-COF).

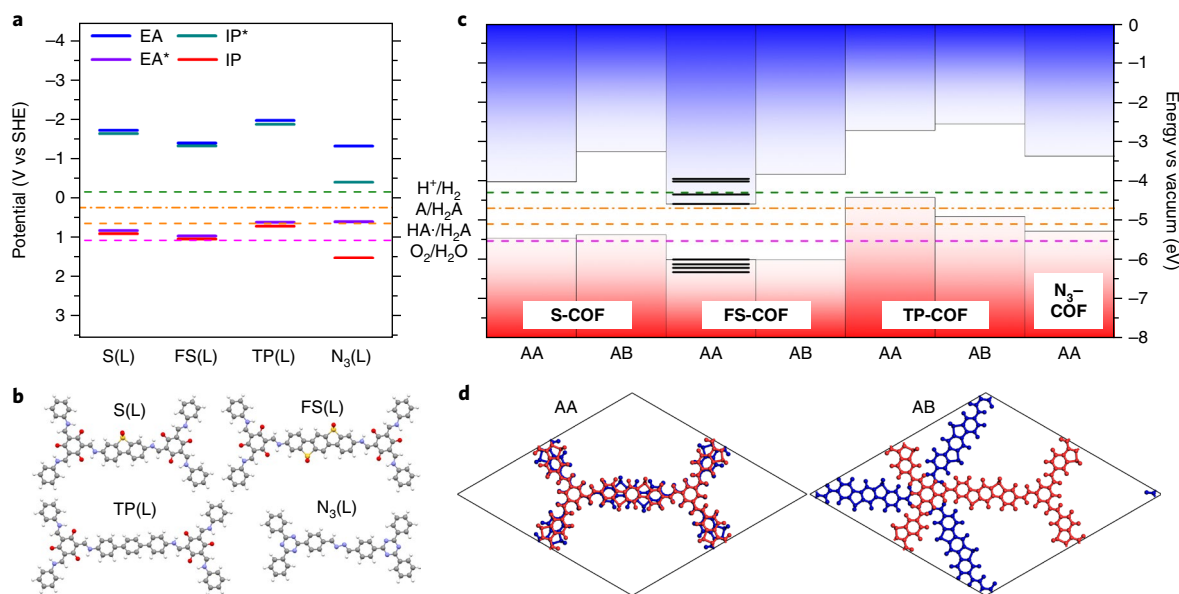


**Fig. 5 | Electronic structure calculations provide insights into the photocatalytic water splitting activities of the COFs.** **a,b**, (TD-)B3LYP predicted IP, EA, IP\* and EA\* adiabatic potentials (**a**) of representative fragments of the different COFs (**b**) in water; S(L), FS(L), TP(L) and N<sub>3</sub>(L) are representative fragments of S-COF, FS-COF, TP-COF and N<sub>3</sub>-COF, respectively. **c,d**, Periodic DFT (HSE06) predicted VBM (red) and CBM (blue) of the COFs with respect to a common vacuum level (**c**). Both eclipsed (AA) and staggered (AB) stacking arrangements (**d**) were considered. For **FS-COF**, multiple AA-stacked structures were generated, with the calculated VBM and CBM for each individual stacking shown as black horizontal lines in **c**, for which the assignment is shown in Supplementary Fig. 93. Dashed coloured lines in **a** and **c** indicate the potentials for different solution reactions: green, proton reduction; orange, two-hole (A/H<sub>2</sub>A) and one-hole (HA/H<sub>2</sub>A) oxidation of ascorbic acid; magenta, overall water oxidation. All solution potentials shown are for pH 2.6, the experimentally measured pH of a 0.1 M ascorbic acid solution.

Eosin Y has a similar absorption spectrum to **FS-COF**, so it does not harvest additional photons in the energy-rich near-infrared region of the solar spectrum where **FS-COF** does not absorb. A greater enhancement in the HER was observed when a near-infrared absorbing dye, **WS5F**, was used. Unlike the previous dyes, **WS5F** does not dissolve well in water, so it was pre-loaded into the COF using acetone before the photocatalytic tests (loading conditions: 5 mg **FS-COF** + 5 mg **WS5F**). When 5 mg of this dye-sensitized material, **FS-COF**+**WS5F** was used, we observed a visible-light HER of 16.3 mmol g<sup>-1</sup> h<sup>-1</sup>, again normalized to the mass of the COF. We ascribe this enhancement to the absorption of more photons at higher wavelengths by the dye-loaded composite, as expressed in the EQE at 600 and 700 nm when using monochromatic light. At 600 nm, **FS-COF** has an EQE of 0.6%, which is increased to 2.2% for the **FS-COF**+**WS5F** composite. At 700 nm, the composite has an EQE of 0.7%, while **FS-COF** is completely inactive.

We attribute the dye sensitization effect to host–guest interactions in the large, hydrophilic 1D mesopore channels (Supplementary Fig. 94), which may help to explain why dye sensitization with Eosin Y and **WS5F** was unsuccessful for the less porous **FS-P** material. Control experiments using the neat dyes, Eosin Y and **WS5F**, in the absence of **FS-COF**, showed negligible hydrogen production under visible light (0.1 M ascorbic acid solution plus Pt). Similarly, **WS5F** supported on mesoporous silica (SBA-15) showed no hydrogen evolution under the same conditions.

The photoluminescence spectra of **FS-COF**+**WS5F** were measured to investigate the interaction between **FS-COF** and **WS5F**. As shown in Supplementary Fig. 70, **WS5F** solution in acetone excited at 410 nm exhibits an intense emission peak at 630 nm, which can be quenched by increasing the concentration of colloidal **FS-COF**. As there is no obvious overlap between the absorption spectrum of **FS-COF** and the photoluminescence emission of **WS5F**, the fluorescence quenching in **WS5F**+**FS-COF** is likely to be the result of interfacial electron transfer from the excited dye to **FS-COF**. This is supported by calculations that suggest a favourable energy alignment

(Fig. 6d): for example, one possible scheme is that the photoexcited dye transfers electrons to **FS-COF** and is then regenerated by the sacrificial electron donor<sup>53</sup>.

**Photocatalysis experiments with thin COF films.** Sacrificial hydrogen production is a step on the path to overall water splitting, but the latter may require the construction of more sophisticated architectures, such as Z schemes<sup>54–56</sup>. Z schemes comprise two separate, coupled semiconductor phases, where each phase carries out one of the half-reactions in overall water splitting. To create such architectures, processability is important<sup>57</sup>. We found that **FS-COF** can be dispersed as a colloidal solution in various solvents (Fig. 6f), and we used this to dropcast platinized **FS-COF** onto glass supports. Photocatalytic HERs ( $\lambda > 420$  nm, 0.1 M ascorbic acid, 5 h irradiation) were found to increase with the number of dropcasting cycles (Supplementary Fig. 84), presumably due to increased film thickness, to up to 24.9 mmol h<sup>-1</sup> m<sup>-2</sup> after 20 successive depositions of the colloidal solution. Longer-term hydrogen evolution experiments for a COF film produced with just a single dropcast cycle showed steady hydrogen production over 20 hours, indicating that the film was stable under the reaction condition ( $\lambda > 420$  nm, 0.1 M ascorbic acid) (Fig. 6e). We also tested hydrogen evolution of this film under solar simulator irradiation (AM1.5G, classification ABA, ASTM E927-10), which gave a HER of 15.8 mmol h<sup>-1</sup> m<sup>-2</sup> (~0.361 h<sup>-1</sup> m<sup>-2</sup>). This can be compared with data obtained at laboratory scale for carbon nitride films (0.191 h<sup>-1</sup> m<sup>-2</sup>)<sup>58</sup>. Scanning electron micrographs (Supplementary Fig. 81) show that these COF films had smooth, uniform morphologies, and AFM analysis (Supplementary Fig. 82) indicates that the film, after one dropcasting cycle, is ~10 nm thick.

## Conclusions

Although crystallinity is not required for all applications of porous materials<sup>59</sup>, here we see a dramatic enhancement in photocatalytic HERs for ordered, crystalline COFs over structurally related amorphous or semicrystalline solids. Organic building blocks that

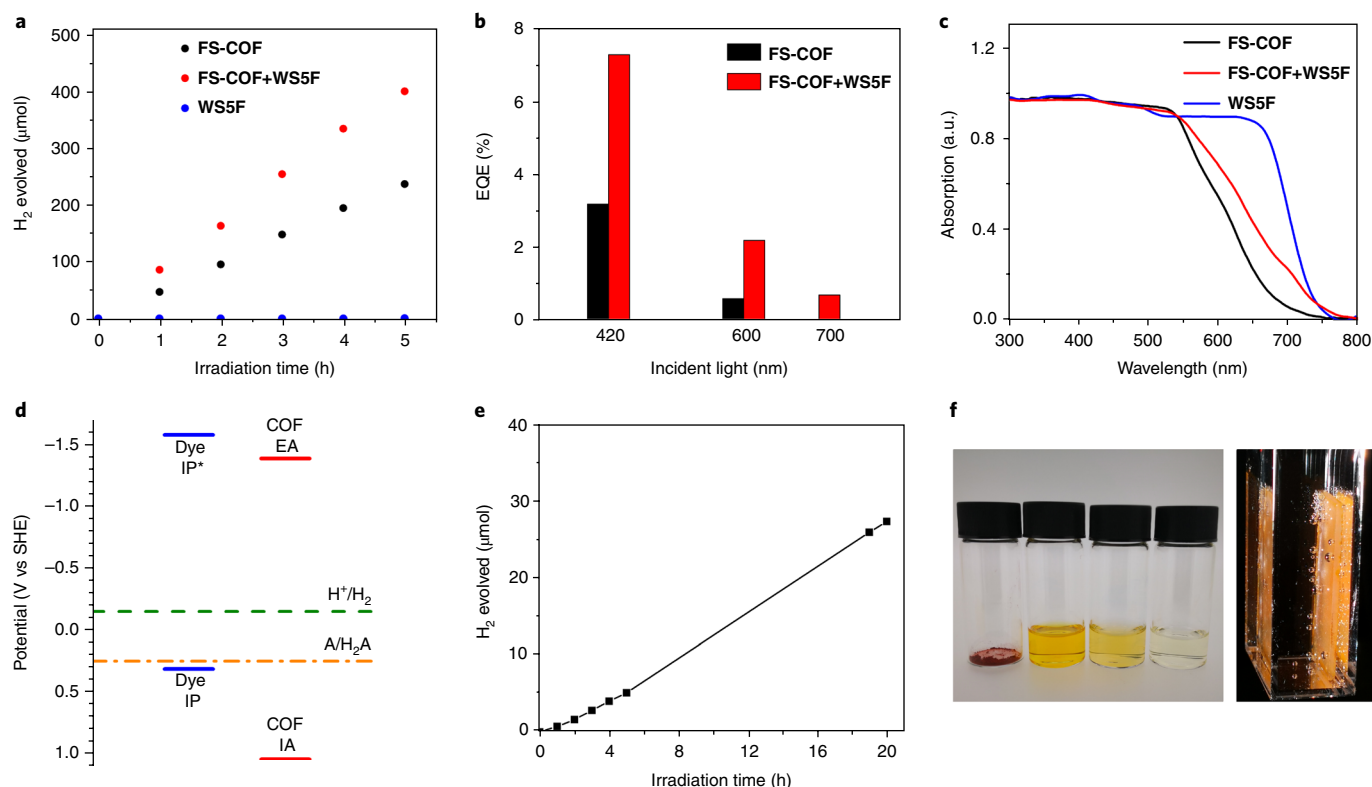


**Fig. 6 | Dye sensitization of FS-COF and hydrogen evolution from an FS-COF film. a**, Time course for photocatalytic  $H_2$  production using visible light for FS-COF, a neat, near-infrared dye (WS5F) and a dye-sensitized COF (FS-COF+WS5F); 5 mg material in water, 5  $\mu\text{l}$  (8 wt%  $H_2PtCl_6$ ), 0.1 M ascorbic acid,  $\lambda > 420$  nm. **b**, EQEs at three different incident light wavelengths for FS-COF and FS-COF+WS5F (5 mg catalyst in water, 5  $\mu\text{l}$  (8 wt%  $H_2PtCl_6$ ), 0.1 M ascorbic acid,  $\lambda = 420 \pm 10$ ,  $\lambda = 600 \pm 45$  and  $700 \pm 10$  nm irradiation; Supplementary Fig. 43). **c**, Solid-state UV-vis spectra for FS-COF, WS5F and FS-COF+WS5F. **d**, Relative energy levels as calculated for ascorbic acid, FS-COF and a near-infrared dye, WS5F; dashed green and orange lines indicate potentials for proton reduction and the two-hole oxidation of ascorbic acid in solution, respectively. **e, f**, Photocatalytic  $H_2$  production using FS-COF films: longer-term hydrogen evolution experiments for a COF film produced with a single dropcast cycle (**e**); photographs showing (left to right) solid FS-COF and colloidal dispersions in DMF, water and acetone, respectively (**f**, left; see also Supplementary Figs. 33 and 87) and FS-COF film on glass producing hydrogen (**f**, right) (20 dropcasting cycles, 0.1 M ascorbic acid, solar simulator AM1.5G, class ABA; see also Supplementary Movie 1 with two times original playing speed).

function well in amorphous polymers, such as dibenzo[*b,d*]thiophene sulfone, lead to materials with better catalytic function when incorporated into COFs. A fused building block, benzo[1,2-*b*:4,5-*b'*]bis[*b*]benzothiophene sulfone, forms a COF with a sacrificial HER that exceeds our best linear polymers, P7 and P10, under comparable conditions, and that is also higher than for other reported COFs<sup>32–37</sup>. Because FS-COF is mesoporous, it can be dye-sensitized to give even higher HERs of up to  $16.3 \text{ mmol g}^{-1} \text{ h}^{-1}$ . FS-COF is also stable for at least 50 h of photolysis in water under visible light ( $\lambda > 420$  nm), and can be cast as a colloid onto planar supports to form thin films while still retaining its photocatalytic activity and stability.

Computation suggests that the fine detail of the AA layer stacking in FS-COF, and by analogy other COF materials, may determine the prospects for thermodynamic proton reduction and water oxidation. To improve our understanding of structure–property relationships, it would be helpful to produce COFs with greater degrees of long-range order. Recent synthetic developments, such as seeded growth strategies<sup>60</sup>, offer one way forward.

Proton reduction using a sacrificial electron donor is only the first step towards overall water splitting<sup>61</sup>, but the mesoporous morphology of these COFs, their processability into films, and their high native photocatalytic activity make them attractive platforms for developing hybrid photocatalysts. For example, the internal pore structure of COFs such as FS-COF could be decorated with quantum dots, photoactive organic molecules, fullerenes or single-site

molecular catalysts. COFs with even larger mesopores might be designed to accommodate a second organic or inorganic semiconductor in the pore channels to produce a Z-scheme photocatalyst for overall water splitting<sup>62</sup>.

## Methods

**COF synthesis.** All COFs were prepared using a procedure based on the method described here for the synthesis of FS-COF. A Pyrex tube was charged with 2,4,6-triformylphloroglucinol (10.5 mg, 0.05 mmol), 3,9-diamino-benzo[1,2-*b*:4,5-*b'*]bis[1]benzothiophene-5,5,11,11-tetraoxide (28.8 mg, 0.075 mmol), mesitylene (1.5 ml), 1,4-dioxane (1.5 ml) and aqueous acetic acid (0.3 ml, 6 M). This mixture was homogenized by sonication for 10 min and the tube was then flash-frozen at 77.3 K (liquid  $N_2$  bath) and degassed by three freeze–pump–thaw cycles, before evacuating to a pressure of 100 mtorr. The tube was sealed and then heated at 120 °C for 3 days. The brown precipitate was collected by centrifugation and washed with *N,N*-dimethylformamide (100 ml) and acetone (200 ml). After drying at 120 °C, the product was obtained as a deep red powder (21 mg, 58%). Anal. calcd for  $(C_{30}H_{22}N_2O_8S_2)_n$ : C, 61.42; H, 3.78; N, 4.78; S, 10.93. Found: C, 44.80; H, 3.21; N, 3.95; S, 9.93.

**Dye sensitization.** For water-insoluble dyes such as WS5F, the dye was loaded into the COF using an organic solvent before hydrogen evolution experiments. To do this, 5 mg WS5F was dissolved in 10 ml acetone and then 5 mg FS-COF was added to the solution and stirred for 12 h. The resulting mixture was filtered, and the filtrate was dried at 80 °C overnight. Amorphous FS-P was loaded with WS5F in the same way. For water-soluble dyes, the dye was added directly into the photocatalytic mixture. In a typical procedure, a flask was charged with COF powder (or amorphous polymer) (5 mg), aqueous 0.1 M ascorbic acid solution (25 ml) and hexachloroplatinic acid (5  $\mu\text{l}$ , 8 wt% aqueous solution). In the case of dye sensitization experiments with water-soluble dyes (Eosin Y, 2',



7'-dichlorofluorescein or Rose Bengal), the dye was added directly to the flask. HERs were normalized to the mass of the COF (or amorphous polymer) in all cases.

**Hydrogen evolution experiments.** A flask was charged with the photocatalyst powder (5 mg), 0.1 M ascorbic acid water solution (25 ml), hexachloroplatinic acid (5  $\mu$ l, 8 wt% aqueous solution) as a Pt precursor and water-soluble dye (if any). The resulting suspension was ultrasonicated for 20 min before degassing by  $N_2$  bubbling for 30 min. The reaction mixture was illuminated with a 300 W Newport Xe light source (model 6258, ozone-free) for the period specified, using appropriate filters. The lamp was cooled by water circulating through a metal jacket. Gas samples were taken with a gas-tight syringe and analysed using a Bruker 450-GC gas chromatograph (GC). Hydrogen was detected with a thermal conductivity S3 detector referencing against a standard gas of known concentration. Hydrogen dissolved in the reaction mixture was not measured and the pressure increase generated by the evolved hydrogen was neglected in the calculations. The rates were determined from a linear regression fit. After 5 h of photocatalysis, no carbon monoxide associated with framework or ascorbic acid decomposition could be detected on a GC system equipped with a pulsed discharge detector. After the photocatalysis experiment, the FS-COF was recovered by washing with water and acetone before drying at 120 °C.

**Calculations.** For the different molecular fragments representing the COFs, we calculated the standard reduction potentials of half-reactions for free electrons/holes and excitons, using DFT and time-dependent DFT (TD-DFT). The B3LYP<sup>63,64</sup> density functional was used for all DFT and TD-DFT calculations (unless otherwise stated), together with the Def2-SVP basis set<sup>65</sup>, using Gaussian 16 software<sup>66</sup>. S1 optimizations for calculations of exciton potentials (IP\* and EA\*) used the Tamm–Dancoff approximation<sup>67</sup>. The effect of solvation by water was accounted for using the PCM/SMD solvation model<sup>68,69</sup>. The potentials of the solution reactions for one- and two-hole oxidation of ascorbic acid were calculated as described in Supplementary Section 22, while the experimental values were used for the proton reduction and water oxidation reactions.

Periodic DFT calculations on the COF crystal structures were carried out within the plane-wave pseudopotential formalism, using the Vienna ab initio Simulation Package (VASP) code<sup>70</sup>. Geometry optimizations were performed with the Perdew–Burke–Ernzerhof exchange–correlation functional with the DFT-D3(BJ) dispersion correction<sup>71–73</sup>. A kinetic-energy cutoff of 500 eV was used to define the plane-wave basis set. The electronic structure of each optimized COF structure was then computed using a screened hybrid exchange–correlation functional (HSE06)<sup>74–76</sup>, giving key electronic properties, such as bandgap and electrostatic potential. To achieve valence band alignment so that band energies could be compared for the different COF structures, we followed an approach devised for determining the vacuum level of porous structures<sup>77</sup>. Further computational details are provided in Supplementary Section 22.

## Data availability

Crystallographic data for the structures reported in this Article have been deposited at the Cambridge Crystallographic Data Centre, under deposition nos. CCDC 1818058 (fused sulfone diamine, FSA) and 1818059 (sulfone diamine, SA). Copies of the data can be obtained free of charge from [www.ccdc.cam.ac.uk/structures/](http://www.ccdc.cam.ac.uk/structures/). All other data supporting the findings of this study are available within the Article and its Supplementary Information and/or from the corresponding authors upon reasonable request.

Received: 2 May 2018; Accepted: 13 August 2018;  
Published online: 1 October 2018

## References

- Fujishima, A. & Honda, K. Electrochemical photolysis of water at a semiconductor electrode. *Nature* **238**, 37–38 (1972).
- Kudo, A. & Miseki, Y. Heterogeneous photocatalyst materials for water splitting. *Chem. Soc. Rev.* **38**, 253–278 (2009).
- Sivula, K. & van de Krol, R. Semiconducting materials for photoelectrochemical energy conversion. *Nat. Rev. Mater.* **1**, 15010 (2016).
- Chen, S., Takata, T. & Domen, K. Particulate photocatalysts for overall water splitting. *Nat. Rev. Mater.* **2**, 17050 (2017).
- Wang, X. et al. A metal-free polymeric photocatalyst for hydrogen production from water under visible light. *Nat. Mater.* **8**, 76–80 (2009).
- Sprick, R. S. et al. Tunable organic photocatalysts for visible-light-driven hydrogen evolution. *J. Am. Chem. Soc.* **137**, 3265–3270 (2015).
- Zhang, G., Lan, Z.-A. & Wang, X. Conjugated polymers: catalysts for photocatalytic hydrogen evolution. *Angew. Chem. Int. Ed.* **55**, 2–18 (2016).
- Yanagida, S., Kamamoto, A., Mizumoto, K., Pac, C. & Yoshino, K. Poly(para)phenylene-catalyzed photoreduction of water to hydrogen. *Chem. Commun.* **8**, 474–475 (1985).
- Shibata, T. et al. Novel visible-light-driven photocatalyst. Poly(*p*-phenylene)-catalyzed photoreductions of water, carbonyl compounds, and olefins. *J. Phys. Chem.* **94**, 2068–2076 (1990).
- Schwinghammer, K. et al. Crystalline carbon nitride nanosheets for improved visible-light hydrogen evolution. *J. Am. Chem. Soc.* **136**, 1730–1733 (2014).
- Schwab, M. G. et al. Photocatalytic hydrogen evolution through fully conjugated poly(azomethine) networks. *Chem. Commun.* **46**, 8932 (2010).
- Yang, C. et al. Molecular engineering of conjugated polybenzothiadiazoles for enhanced hydrogen production by photosynthesis. *Angew. Chem. Int. Ed.* **55**, 9202–9206 (2016).
- Li, L. et al. Rational design of porous conjugated polymers and roles of residual palladium for photocatalytic hydrogen production. *J. Am. Chem. Soc.* **138**, 7681–7686 (2016).
- Woods, D. J., Sprick, R. S., Smith, C. L., Cowan, A. J. & Cooper, A. I. A solution-processable polymer photocatalyst for hydrogen evolution from water. *Adv. Energy Mater.* **7**, 1700479 (2017).
- Sprick, R. S. et al. Extended conjugated microporous polymers for photocatalytic hydrogen evolution from water. *Chem. Commun.* **52**, 10008–10011 (2016).
- Sprick, R. S. et al. Visible-light-driven hydrogen evolution using planarized conjugated polymer photocatalysts. *Angew. Chem. Int. Ed.* **55**, 1792–1796 (2016).
- Wang, K. et al. Covalent triazine frameworks via a low temperature polycondensation approach. *Angew. Chem. Int. Ed.* **56**, 14337–14341 (2017).
- Meier, C. B. et al. Structure–property relationships for covalent triazine-based frameworks: the effect of spacer length on photocatalytic hydrogen evolution from water. *Polymer* **126**, 283–290 (2017).
- Bi, J. et al. Covalent triazine-based frameworks as visible light photocatalysts for the splitting of water. *Macromol. Rapid Commun.* **36**, 1799–1805 (2015).
- Zhang, G., Lan, Z.-A., Lin, L., Lin, S. & Wang, X. Overall water splitting by Pt/C<sub>3</sub>N<sub>4</sub> photocatalysts without using sacrificial agents. *Chem. Sci.* **7**, 3062–3066 (2016).
- Wang, L. et al. Conjugated microporous polymer nanosheets for overall water splitting using visible light. *Adv. Mater.* **29**, 1702428 (2017).
- Zhang, G. et al. Optimizing optical absorption, exciton dissociation, and charge transfer of a polymeric carbon nitride with ultrahigh solar hydrogen production activity. *Angew. Chem. Int. Ed.* **56**, 13445–13449 (2017).
- Coropceanu, V. et al. Charge transport in organic semiconductors. *Chem. Rev.* **107**, 926–952 (2007).
- Ockwig, N. W., Cote, A. P., Keeffe, M. O., Matzger, A. J. & Yaghi, O. M. Porous, crystalline, covalent organic frameworks. *Science* **310**, 1166–1171 (2005).
- El-Kaderi, H. M. et al. Designed synthesis of 3D covalent organic frameworks. *Science* **316**, 268–272 (2007).
- Diercks, C. S. & Yaghi, O. M. The atom, the molecule, and the covalent organic framework. *Science* **355**, eaal1585 (2017).
- Spitler, E. L. et al. Lattice expansion of highly oriented 2D phthalocyanine covalent organic framework films. *Angew. Chem. Int. Ed.* **51**, 2623–2627 (2012).
- Spitler, E. L. & Dichtel, W. R. Lewis acid-catalysed formation of two-dimensional phthalocyanine covalent organic frameworks. *Nat. Chem.* **2**, 672–677 (2010).
- Kandambeth, S. et al. Construction of crystalline 2D covalent organic frameworks with remarkable chemical (acid/base) stability via a combined reversible and irreversible route. *J. Am. Chem. Soc.* **134**, 19524–19527 (2012).
- Huang, N., Wang, P. & Jiang, D. Covalent organic frameworks: a materials platform for structural and functional designs. *Nat. Rev. Mater.* **1**, 16068 (2016).
- Wan, S. et al. Covalent organic frameworks with high charge carrier mobility. *Chem. Mater.* **23**, 4094–4097 (2011).
- Thote, J. et al. A covalent organic framework–cadmium sulfide hybrid as a prototype photocatalyst for visible-light-driven hydrogen production. *Chem. Eur. J.* **20**, 15961–15965 (2014).
- Zhou, J. et al. A (001) dominated conjugated polymer with high-performance of hydrogen evolution under solar light irradiation. *Chem. Commun.* **53**, 10536–10539 (2017).
- Stegbauer, L., Schwinghammer, K. & Lotsch, B. V. A hydrazone-based covalent organic framework for photocatalytic hydrogen production. *Chem. Sci.* **5**, 2789–2793 (2014).
- Vyas, V. S. et al. A tunable azine covalent organic framework platform for visible light-induced hydrogen generation. *Nat. Commun.* **6**, 8508 (2015).
- Haase, F. et al. Structure–property–activity relationships in a pyridine containing azine-linked covalent organic framework for photocatalytic hydrogen evolution. *Faraday Discuss.* **162**, 165–169 (2017).
- Pachfule, P. et al. Diacetylene functionalized covalent organic framework (COF) for photocatalytic hydrogen generation. *J. Am. Chem. Soc.* **140**, 1423–1427 (2018).
- Banerjee, T. et al. Single site photocatalytic H<sub>2</sub> evolution from covalent organic frameworks with molecular cobaloxime co-catalysts. *J. Am. Chem. Soc.* **139**, 16228–16234 (2017).
- Lin, S. et al. Covalent organic frameworks comprising cobalt porphyrins for catalytic CO<sub>2</sub> reduction in water. *Science* **349**, 1208–1213 (2015).
- Sick, T. et al. Oriented films of conjugated 2D covalent organic frameworks as photocathodes for water splitting. *J. Am. Chem. Soc.* **140**, 2085–2092 (2018).

41. Zhu, Y. & Zhang, W. Reversible tuning of pore size and CO<sub>2</sub> adsorption in azobenzene functionalized porous organic polymers. *Chem. Sci.* **5**, 4957–4961 (2014).
42. Kruczynski, L. et al. Porous titania glass as a photocatalyst for hydrogen production from water. *Nature* **291**, 399–401 (1981).
43. Wagner, F. T. & Somorjai, G. A. Photocatalytic hydrogen production from water on Pt-free SrTiO<sub>3</sub> in alkali hydroxide solutions. *Nature* **285**, 559–560 (1980).
44. Corp, K. L., Schlenker, C. W., Corp, K. L. & Schlenker, C. W. Ultrafast spectroscopy reveals electron transfer cascade that improves hydrogen evolution with carbon nitride photocatalysts. *J. Am. Chem. Soc.* **139**, 7904–7912 (2017).
45. Kroeze, J. E., Savenije, T. J., Vermeulen, M. J. W. & Warman, J. M. Contactless determination of the photoconductivity action spectrum, exciton diffusion length, and charge separation efficiency in polythiophene-sensitized TiO<sub>2</sub> bilayers. *J. Phys. Chem. B* **107**, 7696–7705 (2003).
46. Bruno, A., Reynolds, L. X., Dyer-Smith, C., Nelson, J. & Haque, S. A. Determining the exciton diffusion length in a polyfluorene from ultrafast fluorescence measurements of polymer/fullerene blend films. *J. Phys. Chem. C* **117**, 19832–19838 (2013).
47. Shaw, P. E., Ruseckas, A. & Samuel, I. D. W. Exciton diffusion measurements in poly(3-hexylthiophene). *Adv. Mater.* **20**, 3516–3520 (2008).
48. Tezuka, Y., Fukushima, A., Matsui, S. & Imai, K. Surface studies on poly(vinyl alcohol)-poly(dimethylsiloxane) graft copolymers. *J. Colloid Interface Sci.* **114**, 16–25 (1986).
49. Biswal, B. P. et al. Pore surface engineering in porous, chemically stable covalent organic frameworks for water adsorption. *J. Mater. Chem. A* **3**, 23664–23669 (2015).
50. Guiglion, P., Butchosa, C. & Zwiijnenburg, M. A. Polymer photocatalysts for water splitting: insights from computational modeling. *Macromol. Chem. Phys.* **217**, 344–353 (2016).
51. Guiglion, P., Monti, A. & Zwiijnenburg, M. A. Validating a density functional theory approach for predicting the redox potentials associated with charge carriers and excitons in polymeric photocatalysts. *J. Phys. Chem. C* **121**, 1498–1506 (2017).
52. Bach, U. et al. Solid-state dye-sensitized mesoporous TiO<sub>2</sub> solar cells with high photon-to-electron conversion efficiencies. *Nature* **395**, 583–585 (1998).
53. Willkomm, J. et al. Dye-sensitized semiconductors modified with molecular catalysts for light-driven H<sub>2</sub> production. *Chem. Soc. Rev.* **45**, 9–23 (2016).
54. Abe, R., Sayama, K., Domen, K. & Arakawa, H. A new type of water splitting system composed of two different TiO<sub>2</sub> photocatalysts (anatase, rutile) and a IO<sub>3</sub><sup>−</sup>/I<sup>−</sup> shuttle redox mediator. *Chem. Phys. Lett.* **344**, 339–344 (2001).
55. Wang, Q. et al. Scalable water splitting on particulate photocatalyst sheets with a solar-to-hydrogen energy conversion efficiency exceeding 1%. *Nat. Mater.* **15**, 611–615 (2016).
56. Tada, H., Mitsui, T., Kiyonaga, T., Akita, T. & Tanaka, K. All-solid-state Z-scheme in CdS–Au–TiO<sub>2</sub> three-component nanojunction system. *Nat. Mater.* **5**, 782–786 (2006).
57. Goto, Y. et al. A particulate photocatalyst water-splitting panel for large-scale solar hydrogen generation. *Joule* **2**, 509–520 (2018).
58. Schröder, M. et al. Hydrogen evolution reaction in a large-scale reactor using a carbon nitride photocatalyst under natural sunlight irradiation. *Energy Technol.* **3**, 1014–1017 (2015).
59. Slater, A. G. & Cooper, A. I. Function-led design of new porous materials. *Science* **348**, aaa8075 (2015).
60. Evans, A. M. et al. Seeded growth of single-crystal two-dimensional covalent organic frameworks. *Science* **361**, 52–57 (2018).
61. Teets, T. S. & Nocera, D. G. Photocatalytic hydrogen production. *Chem. Commun.* **47**, 9268–9274 (2011).
62. Hisatomi, T., Kubota, J. & Domen, K. Recent advances in semiconductors for photocatalytic and photoelectrochemical water splitting. *Chem. Soc. Rev.* **43**, 7520–7535 (2014).
63. Becke, A.D. Density-functional thermochemistry. III. The role of exact exchange. *J. Chem. Phys.* **98**, 5648–5652 (1993).
64. Stephens, P., Devlin, F., Chabalowski, C. & Frisch, M. J. *Ab initio* calculation of vibrational absorption and circular dichroism spectra using density functional force fields. *J. Phys. Chem.* **98**, 11623–11627 (1994).
65. Weigend, F. & Ahlrichs, R. Balanced basis sets of split valence, triple zeta valence and quadruple zeta valence quality for H to Rn: design and assessment of accuracy. *Phys. Chem. Chem. Phys.* **7**, 3297–3305 (2005).
66. Frisch, M. J. et al. *Gaussian 16 revision A.03* (Gaussian, 2016).
67. Hirata, S. & Head-Gordon, M. Time-dependent density functional theory within the Tamm–Dancoff approximation. *Chem. Phys. Lett.* **314**, 291–299 (1999).
68. Scalmani, G. & Frisch, M. J. Continuous surface charge polarizable continuum models of solvation. I. General formalism. *J. Chem. Phys.* **132**, 114110 (2010).
69. Marenich, A. V., Cramer, C. J. & Truhlar, D. G. Universal solvation model based on solute electron density and a continuum model of the solvent defined by the bulk dielectric constant and atomic surface tensions. *J. Phys. Chem. B* **113**, 6378–6396 (2009).
70. Kresse, G. & Furthmüller, J. Efficient iterative schemes for *ab initio* total-energy calculations using a plane-wave basis set. *Phys. Rev. B* **54**, 11169–11186 (1996).
71. Perdew, J. P., Burke, K. & Ernzerhof, M. Generalized gradient approximation made simple. *Phys. Rev. Lett.* **77**, 3865–3868 (1996).
72. Grimme, S., Antony, J., Ehrlich, S. & Krieg, H. A consistent and accurate *ab initio* parametrization of density functional dispersion correction (DFT-D) for the 94 elements H–Pu. *J. Chem. Phys.* **132**, 154104 (2010).
73. Grimme, S., Ehrlich, S. & Goerigk, L. Effect of the damping function in dispersion corrected density functional theory. *J. Comp. Chem.* **32**, 1456 (2011).
74. Heyd, J., Scuseria, G. E. & Ernzerhof, M. Hybrid functionals based on a screened Coulomb potential. *J. Chem. Phys.* **118**, 8207–8215 (2003).
75. Heyd, J. & Scuseria, G. E. Efficient hybrid density functional calculations in solids: assessment of the Heyd–Scuseria–Ernzerhof screened Coulomb hybrid functional. *J. Chem. Phys.* **121**, 1187–1192 (2004).
76. Heyd, J., Scuseria, G. E. & Ernzerhof, M. Erratum: ‘Hybrid functionals based on a screened Coulomb potential’. *J. Chem. Phys.* **124**, 219906 (2006).
77. Butler, K. T., Hendon, C. H. & Walsh, A. Electronic chemical potentials of porous metal–organic frameworks. *J. Am. Chem. Soc.* **136**, 2703–2706 (2014).

## Acknowledgements

The authors acknowledge funding from the Engineering and Physical Sciences Research Council (EPSRC) (EP/N004884/1), the European Union's Seventh Framework Programme through grant agreement nos. 321156 (ERC-AG-PE5-ROBOT) and 692685, and the Leverhulme Trust via the Leverhulme Research Centre for Functional Materials Design. X.W. thanks the China Scholarship Council for a PhD studentship. Y.W. and W.-H.Z. acknowledge financial support from the NSFC for Creative Research Groups (21421004) and Key Project (21636002), NSFC/China and a Shanghai Oriental Scholarship. The authors thank M. Bilton for help with HR-TEM, F. McBride for help with AFM, and G.-H. Ning and H. Niu for useful discussions. The authors acknowledge the Diamond Light Source for access to beamlines I19 (MT15777) and I11 (EE12336), the ARCHER UK National Supercomputing Service, access provided via a Programme Grant (EP/N004884/1) and the EPSRC funded UK Materials Chemistry Consortium (EP/L000202/1), and the use of the facilities of the N8 HPC Centre of Excellence, provided and funded by the N8 Research Partnership and EPSRC (EP/K000225/1).

## Author contributions

A.I.C. and X.W. conceived the project. X.W. synthesized the COFs and performed the characterization and photocatalysis experiments. L.C. and M.A.Z. conceived the modelling strategy and performed the calculations. S.Y.C. carried out PXRD analyses. M.A.L. carried out single-crystal X-ray structure analysis. R.S.S. performed the TCSPC experiments and co-supervised, with A.I.C., the work on COF synthesis, characterization and photocatalysis. Y.Y. collected the water sorption isotherms. R.C., X.W. and L.C. interpreted the gas sorption isotherms. Y.W. and W.-H.Z. synthesized and characterized the WS5F dye. All authors interpreted the data and contributed to preparation of the manuscript.

## Competing interests

The authors declare no competing interests.

## Additional information

**Supplementary information** is available for this paper at <https://doi.org/10.1038/s41557-018-0141-5>.

**Reprints and permissions information** is available at [www.nature.com/reprints](http://www.nature.com/reprints).

**Correspondence and requests for materials** should be addressed to A.I.C.

**Publisher's note:** Springer Nature remains neutral with regard to jurisdictional claims in published maps and institutional affiliations.

© The Author(s), under exclusive licence to Springer Nature Limited 2018